Clays and Clay Minerals, Vol. 43, No. 3, 304–317, 1995.

CRYSTAL CHEMISTRY OF HYDROUS IRON SILICATE SCALE DEPOSITS AT THE SALTON SEA GEOTHERMAL FIELD

A. MANCEAU,[1] PH. ILDEFONSE,[2] J.-L. HAZEMANN,[1] A-M. FLANK,[3] AND D. GALLUP[4]

[1] Environmental Geochemistry Group, LGIT-IRIGM, University of Grenoble and CNRS, BP53, 38041 Grenoble Cedex 9, France

[2] Laboratoire de Minéralogie et Cristallographie, Tour 16, 4 place Jussieu, 75252 Paris Cedex 05, France

[3] LURE, Bat. 209D, Université Paris-Sud, 91405 Orsay Cedex, France

[4] Unocal Corporation, P.O. Box 76, Brea, California 92621

Abstract—The crystal chemistry of Fe-Si scales deposited from geothermal brines at Salton Sea, California, was studied by powder X-ray diffraction and spectroscopic techniques including infrared, ^{57}Fe Mössbauer, ^{27}Al and ^{29}Si nuclear magnetic resonance (NMR), and Fe and Si K-edge extended X-ray absorption fine structure (EXAFS). Scales precipitated at near 250°C from dissolved ferrous iron and silicic acid are composed of hisingerite. This phase is shown to possess the same local structure as nontronite and is a poorly-crystallized precursor of the ferric smectite. A clear distinction can be made at the local scale between hisingerite and 2-line ferrihydrite because, even in their most disordered states, the former possesses a two-dimensional and the latter a three-dimensional anionic framework. At temperature near 100°C Fe-Si scales are a mix of Al-containing opal and hydrous ferrous silicate, whose local structure resembles minnesotaite and greenalite. This hydrous ferrous silicate is very well ordered at the local scale with an average Fe coordination about Fe atoms of 6 ± 1. The difference in crystallinity between the ferrous and ferric silicate scales was related to variations of growth rates of clay particles precipitated from ferrous and ferric salt solutions. The low crystallinity of the ferric smectite suggests that the oxidation of ferrous iron occurs before polymerization with silica.

Key Words—Crystal chemistry, EXAFS, Ferrihydrite, Hisingerite, Hydrous iron silicate, Mössbauer, NMR.

INTRODUCTION

Over the past decade, considerable effort has been made to generate electricity from steam produced at the Salton Sea geothermal field located in the imperial Valley, southeastern California, USA (Hoyer *et al* 1991). The flashing of steam from hyper-saline brines produces iron-rich siliceous scale deposits that rapidly foul piping and other brine-handling equipment. These scales are brown-black, hard, and vitreous material. Until methods (acidification or crystallization-reaction clarification) were developed to inhibit the formation of these unusual scales, continuous operation of production facilities was drastically hindered. Characterization of the poorly-crystalline, iron-rich silica scale deposits was required to understand the deposition mechanism and to develop techniques to avoid their deposition (Gallup 1989, Gallup and Reiff 1991). These initial studies, using spectroscopic techniques suggested that iron in the scales deposited at high temperature was primarily present in the ferric oxidation state and that the iron silicate phase resembled hisingerite. The present study seeks to determine the chemical environment of iron and silicon in these deposits, with emphasis on determining the possible polyhedral linkages between $Fe(O,OH)_6$ octahedra and SiO_4 tetrahedra. We use several complementary methods, including powder X-ray diffraction, Mössbauer and infrared spectroscopy, ^{27}Al- and ^{29}Si-nuclear magnetic resonance (NMR), and Fe and Si K-edge extended X-ray absorption fine structure spectroscopy (EXAFS).

EXPERIMENTAL

Samples

A series of scale samples precipitated at temperatures ranging from 100–250°C were collected. Three samples were selected for study here because they are pure end-members and not mixtures. S-1, occurring at a brine temperature of near 250°C, consists of a black scale with a vitreous luster and conchoïdal fracture. This sample crystallizes initially around the production wellheads and is observed also several hundred feet down production well casings. S-2 was collected from an injection pump used in a pH modification process which reduces brine pH from 5.5 to 5.0 to inhibit the precipitation of iron (although some residual silica continues to deposit, Hoyer *et al* 1991). The sample is grey in color and precipitated near 180°C. S-3 is an olive-grey filter cake sludge produced in reactor clarifiers. It formed at 100 ± 10°C. Details on the geothermal brine handling equipment, these samples were collected from, can be found in Hoyer *et al* (1991) and Gallup and Featherstone (1994).

Methods

A Philips 1740 diffractometer with a diffracted-beam graphite monochromator was employed for powder XRD. CuKα radiation was used with counting time of 40s per 0.04°/2θ step. Infrared spectroscopy was performed on a FTIR Nicolet 5DX spectrometer. ^{57}Fe Mössbauer spectra were recorded at 300 K with a ^{57}Co/Rh source and native iron was used for velocity calibration. EXAFS measurements were made at the LURE synchrotron radiation laboratory (Orsay, France). Fe K-spectra were collected on the EXAFS IV station at the DCI storage ring and Si K-spectra on the SA32 station at the Super ACO storage ring. EXAFS data were reduced using the plane-wave approximation and a standard procedure (Teo 1986). Interatomic distances were calculated using theoretical (McKale *et al* 1988) and experimental phase shift (ϕ) and amplitude functions (F). γFeOOH was used as a reference compound for analyzing Fe-Fe atomic pairs. $\phi_{Fe\text{-}Fe}$ and $F_{Fe\text{-}Fe}$ were determined considering the following structural parameters for γFeOOH: d(Fe-Fe) = 3.06 Å, a number of 6 nearest Fe neighbors (N_{Fe}), and a Debye Waller term (σ) of 0.08 Å (Oles *et al* 1970). ^{27}Al and ^{29}Si NMR spectra were recorded using in-house Fourier-transform NMR spectrometers based on 11.7T and 8.45T superconducting solenoids and automated with Nicolet 1280 computer system. The ^{27}Al NMR spectra were collected at Ho = 11.7T (130.3 MHz ^{27}Al Larmor frequency) under magic angle-spinning (MAS) conditions at spinning frequencies of 11 kHz. At this spinning rate, the spinning sidebands do not overlap true peaks and their positions are outside the range of isotropic ^{27}Al chemical shifts in aluminosilicates. The ^{27}Al chemical-shifts values at the maximum intensity, δ_p, are expressed relative to an external standard of 1 M $Al(H_2O)Cl_3$ in H_2O. The ^{29}Si NMR spectra were collected at Ho = 8.45T (71.514 MHz ^{29}Si Larmor frequency) at a spinning frequency of 3.2 kHz. The ^{29}Si chemical-shifts values at the maximum intensity, δ_p, are reported relative to external tetramethylsilane. In all spectra presented here, more negative shifts (towards the right) correspond to increased shielding and lower frequency.

RESULTS

Chemical analyses

Chemical bulk compositions are reported in Table 1. These analyses correspond well to previously published analyses (Gallup and Reiff 1991). S-1 contains predominantly Si and Fe with a Fe/Si mole ratio of 0.7. S-2 is highly depleted in iron (Fe/Si = 0.01) due to brine acidification, but is enriched in Al. S-3 has an intermediate composition with Fe/Si = 0.08. These samples were analyzed also by electron microprobe and major element concentrations are reported in the triangular diagram of Figure 1. At the resolution of the microprobe ($\approx$10 μm^3), S-1 and S-3 are homogeneous in composition but not S-2 where Fe_2O_3 and Al_2O_3 content and Fe/Si ratio vary between 0–7%, 3–13% and 0.0–0.08, respectively. A typical analysis of Salton Sea brines was given by Gallup (1993).

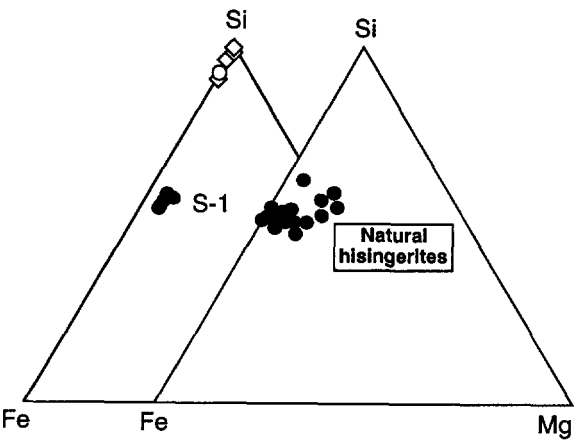

Figure 1. Si-Fe-Mg triangular plot of chemical analyses for scale samples (left diagram) compared to natural hisingerites (right diagram; from Brigatti 1982, Eggleton *et al* 1983, Shayan 1984). Left diagram: filled circle = microprobe analyses for S-1; open diamond = microprobe analyses for S-2; open circle = bulk analyses for S-3.

XRD

XRD patterns of the various scale samples are given in Figure 2. The XRD trace of S-1 closely resembles those of natural hisingerite (Kohyama and Sudo 1975, Eggleton 1988, Shayan 1984) and synthetic ferric smectite (Decarreau *et al* 1987, Mizutani *et al* 1991, Farmer *et al* 1994). A broad 001 basal reflection occurs at near 5° 2θ ($\approx$17.7 Å) and two-dimensional *hk* diffraction bands occur near 19.4° 2θ (4.56 Å), 35.6° 2θ (2.61 Å), 53° 2θ (1.7 Å) and 60.3° 2θ (1.53 Å). These features are characteristic of 02-11, 13-20, 15-24-31 and 06-33 diffraction bands of a turbostratic layer silicate (Brindley and Brown 1980, Decarreau *et al* 1987). The *b* axis based on d (06-33) is 9.20 Å, which corresponds to

Table 1. Bulk chemical analyses of major elements in scale samples.

Sample	SiO_2	Al_2O_3	Fe_2O_3	MnO	MgO	OaO	Na_2O	Total	Fe^{3+}/Si
S-1	42.16	2.72	40.32	0.18	1.99	1.37	0.24	88.98	0.72
S-2	78.67	8.22	1.48	0.07	0.13	0.64	1.25	90.46	0.01
S-3	83.46	<0.1	8.86	0.49	<0.1	0.29	0.26	93.36	0.08

https://doi.org/10.1346/CCMN.1995.0430305 Published online by Cambridge University Press

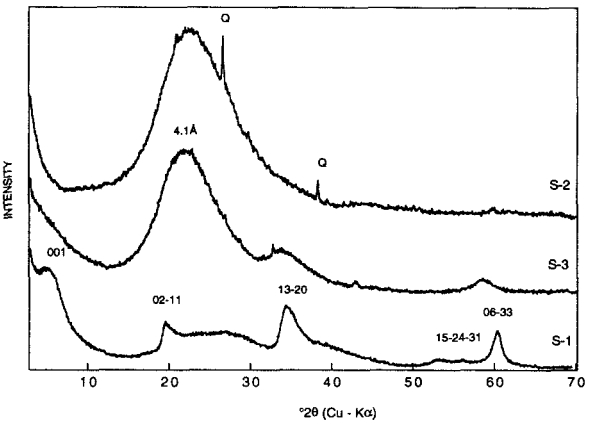

Figure 2. XRD patterns for scale samples. Q = quartz.

hisingerite (Whelan and Goldich 1961) and nontronite (Eggleton 1977). This XRD pattern also displays a broad diffuse band near 25–27° 2θ (3.6–3.3 Å), which was tentatively attributed to adsorbed water by Decarreau *et al* (1987), but which probably is the 004 reflection of a ferric smectite (e.g., see Mizutani *et al* 1991). The presence of amorphous silica is unlikely because it has a scattering band at 22–23° 2θ (3.9–4.2 Å). Likewise, this scattering feature cannot be assigned to Si-rich ferrihydrite component, which has a broad scattering band near 2.7–2.9 Å (Vempati and Loeppert 1985, 1989, Childs *et al* 1990). The XRD trace for S-2 has an intense scattering band centered at 22–23° 2θ, which is characteristic of A-opal. S-3 also has a broad scattering band centered at 22–23° 2θ, but in addition to S-2, two broad features at 32.9° 2θ (2.7 Å) and 58.8° 2θ (1.57 Å) are observed also. Quartz is present at trace level.

Mössbauer spectroscopy

Mössbauer spectra for each sample was recorded at room temperature (Figure 3). Values of isomer shift (δ/Fe), quadrupole splitting (ΔE_Q), and line width (W) are presented in Table 2. They were determined by least-square curve fitting, assuming that the iron components exhibit one or two Lorentzian peaks.

As a first step, the Mössbauer spectra were fitted by using two Lorentzian doublets with Mössbauer parameters characteric of octahedral Fe(III) and Fe(II) (Coey 1984, 1988) (Table 2). S-1 yields an intense Fe(III) doublet (95%), characterized by an isomer shift of 0.36 mm·s^{-1} and a quadrupole splitting of 0.85 mm·s^{-1}. The second Fe(II) doublet (5%) has an isomer shift of 0.99 mm·s^{-1} and a quadrupole splitting of 2.51 mm·s^{-1}. S-2 (Figure 3b) is characterized by an intense Fe(II) doublet (70%) (δ/Fe = 1.10 mm·s^{-1} and ΔE_Q = 2.52 mm·s^{-1}) and a Fe(III) doublet (30%), with an isomer shift of 0.40 mm·s^{-1} and a quadupole splitting of 0.73 mm·s^{-1}. The S-3 spectrum has a very intense Fe(II) doublet (96%) characterized by an isomer shift of 1.11

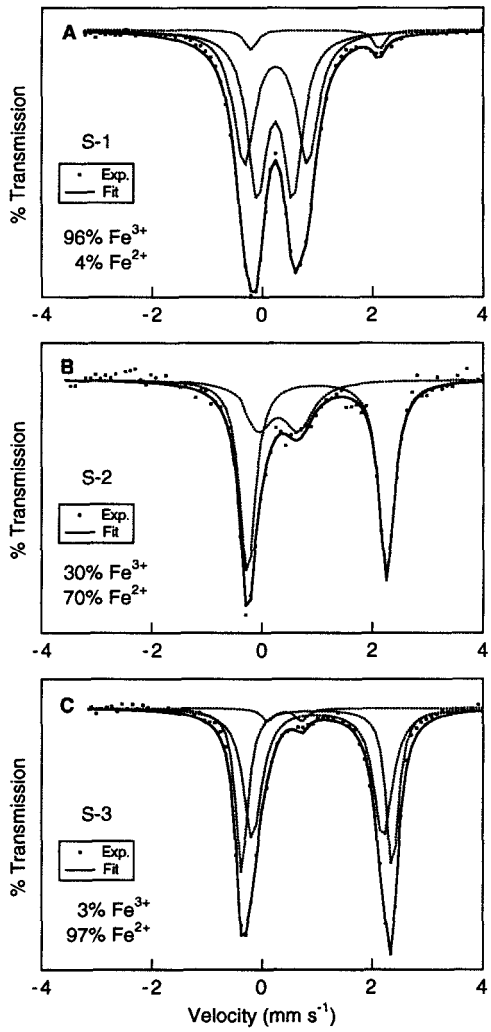

Figure 3. Mössbauer spectra for scale samples.

mm·s^{-1} and a quadrupole splitting of 2.59 mm·s^{-1}, and a Fe(III) doublet (4%), with an isomer shift of 0.48 mm·s^{-1} and a quadrupole splitting of 0.65 mm·s^{-1}.

In a second fitting procedure, a two-doublet fit model was used to simulate octahedral Fe(III) and octahedral Fe(II) sites in S-1 and S-3 (Figures 3a and 3c). Note that two-doublet fits are classically used for fitting spectra of Fe-Si oxides and silicates, as with smectite (Rozenson and Heller-Kallai 1977, Bonnin *et al* 1985, Decarreau *et al* 1987) and hisingerite (Eggleton *et al* 1983). The necessity of a second doublet for Fe sites is required by the existence of distorted, non-equivalent cristallographic sites. These two-doublet fits require elementary doublets which differ by their quadrupole splittings. For example, the decomposition of the single Fe(III) doublet in S-1 (ΔE_Q = 0.85 mm·s^{-1}, Table 2) leads to two doublets whose ΔE_Q are equal to 0.66 mm·s^{-1} and 1.14 mm·s^{-1}. These values are close to those

https://doi.org/10.1346/CCMN.1995.0430305 Published online by Cambridge University Press

Table 2. Computed Mössbauer parameters of scales studied at 295 K.

Sample	δ/Fe	ΔE_Q	W	Intensity %	Attribution	
S-1	0.36	0.85	0.56	95	$Fe(III)_{Oct.}$	Two doublet-fit
	0.99	2.51	0.29	5	$Fe(II)_{Oct.}$	
	0.35	0.66	0.53	50.4	$Fe(III)_{Oct.}$	Three doublet-fit
	0.36	1.14	0.46	45.6	$Fe(III)_{Oct.}$	
	1.07	2.34	0.25	4	$Fe(II)_{Oct.}$	
S-2	0.40	0.73	0.62	30	$Fe(III)_{Oct.}$	Two doublet-fit
	1.10	2.52	0.33	70	$Fe(II)_{Oct.}$	
S-3	0.48	0.65	0.23	4	$Fe(III)_{Oct.}$	Two doublet-fit
	1.11	2.59	0.39	96	$Fe(II)_{Oct.}$	
	0.52	0.60	0.26	3	$Fe(III)_{Oct.}$	Three doublet-fit
	1.12	2.37	0.39	53	$Fe(II)_{Oct.}$	
	1.11	2.73	0.26	44	$Fe(II)_{Oct.}$	

Isomer shift (δ/Fe), Quadrupole splitting (ΔE_Q) and line width (W) given in $mm \cdot s^{-1}$ and relative to iron foil.

of natural hisingerite from Mexico (δ/Fe = 0.41, ΔE_Q = 0.65 $mm \cdot s^{-1}$ and 1.17 $mm \cdot s^{-1}$) (McKenzie and Berezowski 1980) but ΔE_Q values are larger than those of nontronite (0.23–0.70 $mm \cdot s^{-1}$) (Goodman *et al* 1976, Bonnin *et al* 1985, Cardile and Johnston 1985). In S-3, two doublets were used also to simulate the octahedral Fe(II). The values of the isomer shift for each doublet are 1.11–1.12 $mm \cdot s^{-1}$ and the two values of the quadrupole splitting are 2.73 ± 0.01 $mm \cdot s^{-1}$ and 2.37 ± 0.01 $mm \cdot s^{-1}$.

Mössbauer analysis shows that the samples can be distinguished by their variation in Fe(II) and Fe(III) contents: iron is trivalent in the Fe-rich scale precipitated at high temperature (S-1), divalent and trivalent in the Si-rich scale precipitated at intermediate temperature (S-2) and divalent in the Si-rich scale precipitated at low temperature (S-3). These results are in agreement with those reported by Gallup (1989) which indicated that scales are more ferrous as their deposition temperature decreases (S-1: 252°C, S-2: 182°C, S-3: 100°C).

Infrared spectroscopy

IR spectra for the samples are presented in Figure 4, along with nontronite. The spectrum for S-1 is similar to those published for natural hisingerites (MacKenzie and Berezowski 1980, Kohyama and Sudo 1975, Shayan 1984), and resembles that for nontronite, which confirms our XRD interpretation regarding the mineralogical nature of the Fe-rich scale precipitated at high temperature. The strong band at 1010–1030 cm^{-1} observed in S-1 deserves special attention because its position has been explained previously by the existence Si-O-Fe bonds in Fe-Si hydrous oxides and silicates (Schwertmann and Thalmann 1976, Carlson and Schwertmann 1981, Vempati and Loeppert 1989, Gallup and Reiff 1991). The hisingerite spectrum differs from nontronite by the absence of libration OH bands near 800 cm^{-1} or their very weak absorbance when present (Kohyama and Sudo 1975). In natural nontronite, up to three of these bands can be observed at 785 cm^{-1}, 817 cm^{-1}, and 846 cm^{-1}, which were attributed to FeMgOH, FeFeOH, and AlFeOH groups, respectively (Goodman *et al* 1976).

Spectra for Si-rich scales resemble that of opal (Webb and Finlayson 1987) displaying an antisymmetric Si-O-Si stretching band at 1095–1106 cm^{-1} and a symmetric Si-O-Si band at 780–792 cm^{-1} (Moenke 1974). The antisymmetric band of S-2 lies at 1095 cm^{-1}. In tectosilicates, this band shifts to lower wavenumbers with increasing lattice substitution of tetrahedral Al (Milkey 1960, Webb and Finlayson 1987). In opals, this peak varies from 1100 cm^{-1} (no Al) to 1090 cm^{-1} (Al-opal). Thus the value found for S-2 suggests the presence of 4-fold coordinated Al in the opal framework. This evidence is consistent with the microprobe analysis, which showed that the Al_2O_3 content may be as high as 13%, and results obtained by ^{27}Al NMR.

^{27}Al- and ^{29}Si-NMR spectroscopy

Si-rich S-2 was studied by ^{27}Al and ^{29}Si NMR spectroscopy. The ^{27}Al NMR spectrum yields a single res-

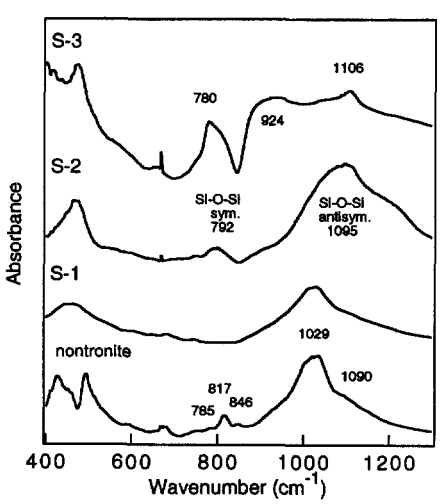

Figure 4. IR spectra for scale samples and nontronite.

https://doi.org/10.1346/CCMN.1995.0430305 Published online by Cambridge University Press

onance with an apparent maximum at δ ppm = 53.7 ppm (Figure 5a). This value is characteristic of tetrahedrally coordinated Al (Müller *et al* 1981). The resonance near −30 ppm ("ssb," Figure 5a) is a spinning side band. The ^{29}Si NMR spectrum of S-2 exhibits a large peak centered around −110 ppm with a full width at half maximum (FWHM) of 17.6 ppm (Figure 5b). This chemical shift corresponds to Si atoms coordinated to four oxygens in a three dimensional array of corner-sharing tetrahedra (Lippmaa *et al* 1980, De Jong *et al* 1987). The assymmetry towards less negative values indicates that the chemical environment about the Si tetrahedra is not unique. This spectrum was decomposed into three Gaussian components at −111.84, −104.75 and −98.85 ppm. These values correspond well to those expected for Si tetrahedra bridged to 4Si, 3Si + 1Al, and 2Si + 2Al, respectively (Lippmaa *et al* 1980). The broadness of NMR peaks in opal arises from the spread of Si-O-Si angles (De Jong *et al* 1987).

EXAFS spectroscopy

Fe K-EXAFS. EXAFS spectra for S-1 and S-3 bear no resemblance, which indicates that Fe atoms are in a different structural environment in these two samples (Figure 6). The shape and phase of the S-1 spectrum

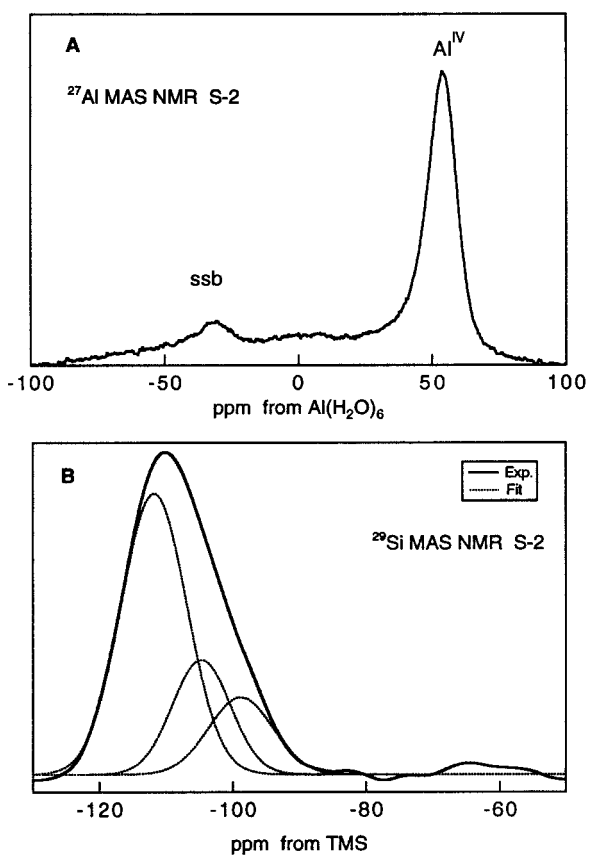

Figure 5. ^{27}Al and ^{29}Si NMR spectra for sample S-2.

closely match those of nontronite. The most prominent difference between S-1 and nontronite spectra is the amplitude lowering of the former, which is an indication of structural disorder. Radial distribution functions (RDF) are given in Figure 7. Fe-containing scale (S-1, S-3) possess two peaks, the shorter corresponds to the ligand coordination sphere, and the second at larger distance, to Fe-Me (Me = Fe and/or Si) pairings (Manceau 1990). The existence of a relatively intense metal shell peak in S-1 and S-3 is emphasized and points to the presence of a more or less organized second shell and, thus, to a local order extending beyond the first coordination shell. This result implies that Fe-containing scale samples are not as amorphous as the silica sample (S-2, see below). The two RDF peaks of S-1 are, however, markedly lower than those of nontronite, which is consistent with the reduction of amplitude observed in EXAFS spectra. This difference of amplitude affecting both the first and second coordination sphere of the Fe atoms, indicates that hisingerite is more poorly organized than nontronite. Note that the first and second RDF peaks of S-3 are shifted to larger distance indicating an increase of bond lengths. This result is consistent with the presence of divalent iron, as determined by Mössbauer spectroscopy, since the radius of Fe^{2+} is greater than Fe^{3+}.

The contribution of the first and second coordination shells were isolated and Fourier backtransformed to k space to determine structural parameters. The least-squares fitting analysis of the first coordination shells resulted in 6 (O, OH) at 2.00 ± 0.02 Å (σ = 0.12 Å) for S-1 and 6 ± 1 (O, OH) at 2.13 Å ± 0.02 Å (σ = 0.09 Å) for S-2. These distances are consistent with Fe^{3+} and Fe^{2+} occupancy in S-1 and S-3, respectively. However the precision of EXAFS spectroscopy on interatomic distances (≈0.02 Å) and the variation in Fe^{2+} and Fe^{3+} radii are insufficient to determine accurately Fe^{3+}/Fe^{2+} ratios. Thus, Fe^{3+}/Fe^{2+} ratios are provided by Mössbauer spectroscopy.

Fe-Me contributions to EXAFS for S-1 and nontronite are compared in Figure 8. Note the perfect phase correspondence of electronic waves over the wavevector (k) span, differing only by amplitude. This important result indicates that the coordination sphere about Fe is identical in these two solids since the phase of electronic waves depends only on the type of atomic neighbors and the interatomic distances. In phyllosilicate structures, the metal shell contribution is a weighted sum of two elementary contributions originating from atoms located in the octahedral (Fe shell) and tetrahedral (Si shell) sheet (Manceau *et al* 1988, 1990, Manceau 1990). Thus, the electronic wave associated with the Si shell is partly masked by the greater contribution of the octahedral sheet, so that powder EXAFS spectroscopy cannot be used to determine Si neighbors in an unknown structure. For example, the metal shell contribution of nontronite was fitted by

https://doi.org/10.1346/CCMN.1995.0430305 Published online by Cambridge University Press

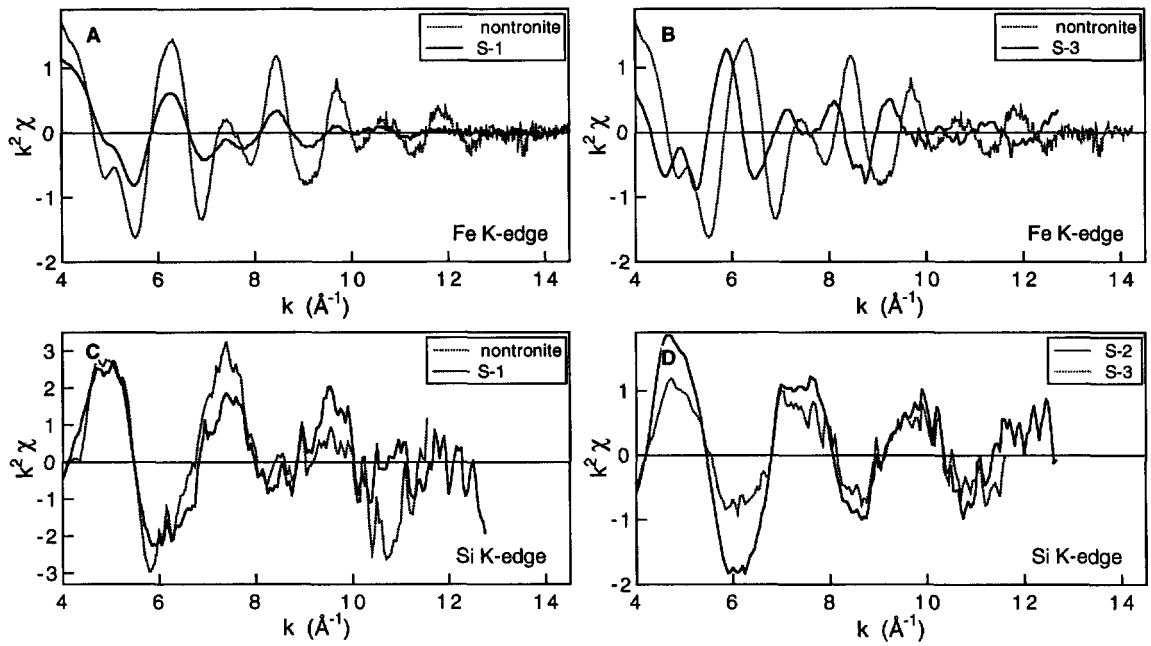

Figure 6. k²-weighted EXAFS spectra for scale samples and nontronite.

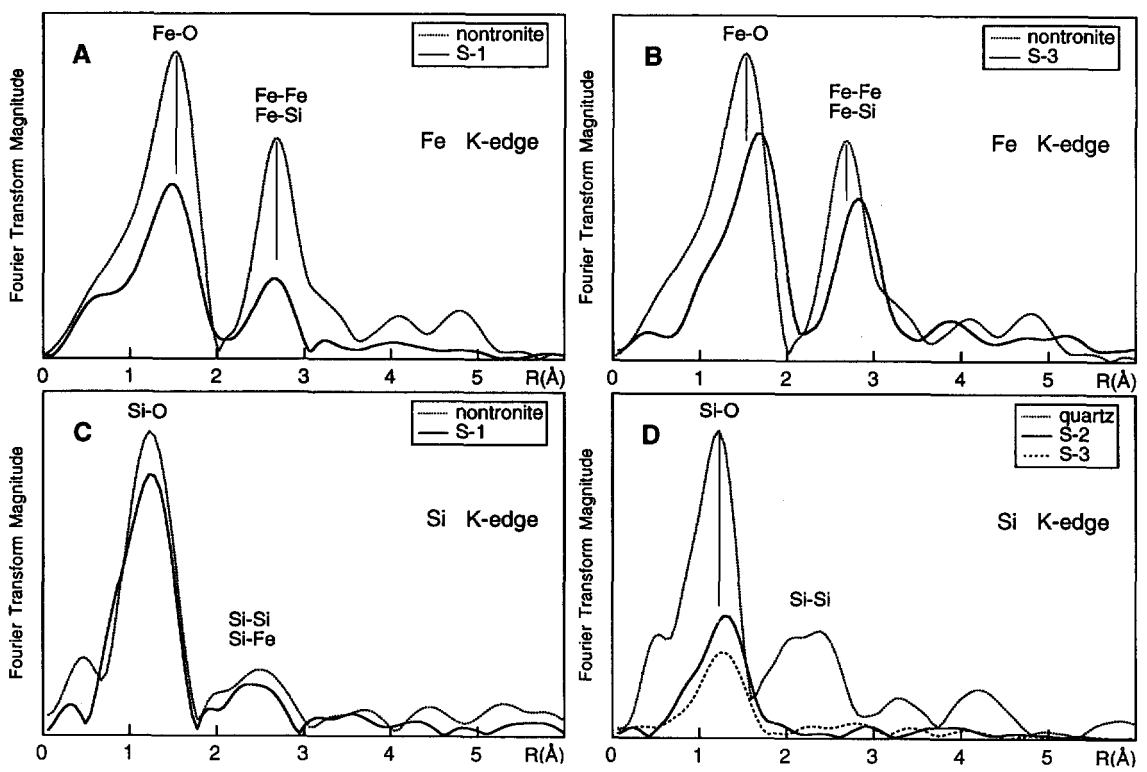

Figure 7. Radial distribution functions (RDFs), uncorrected for phase shifts, produced by the Fourier transform of EXAFS spectra.

https://doi.org/10.1346/CCMN.1995.0430305 Published online by Cambridge University Press

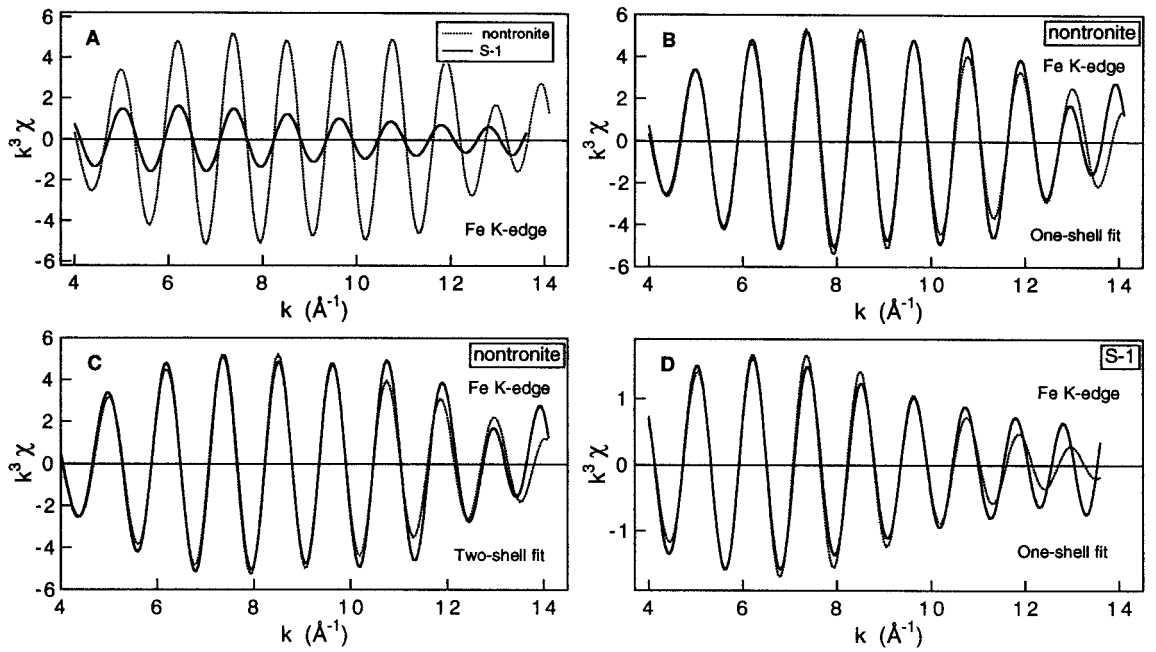

Figure 8. Fourier filtered Fe-(Fe, Si) contributions for nontronite and S-1. a) Experimental spectra; b), c), and d) experimental spectra (solid line) and simulations (dotted line).

assuming either one or two nearest metal shell(s). The single shell fitting of the nontronite spectrum resulted in 6.0 ± 1.0 Fe at 3.07 Å (σ = 0.09 Å) and the two-shell fitting in 3.0 ± 0.6 Fe at 3.07 ± 0.02 Å (σ = 0.08 Å) + 4.0 ± 0.8 Si at 3.24 ± 0.02 Å (σ = 0.07 Å) (Figures 8b and 8c). Observation of Figures 8b and 8c clearly demonstrates that the addition of the Si shell is unnecessary to obtain a good spectral fit. In addition, the two-shell fit is physically meaningless because of the greater number of fitting parameters. Ignoring the Si shell leads to an overestimate of the number of cations in the octahedral sheet by up to 100%, since in dioctahedral clays, octahedral cations have only three nearest octahedral neighbors. Knowing the di- or trioctahedral character of a clay mineral is a prerequisite for correctly analyzing its EXAFS spectrum (Manceau 1990).

However, note that adding or omitting the Si shell does not affect the Fe-Fe distance derived from the spectral fitting. Accordingly, the Fe-Fe distance derived from the analysis of the hisingerite spectrum is probably accurate regardless of whether Fe atoms are surrounded by Si atoms. The partial EXAFS contribution of hisingerite was successfully fitted by assuming a single Fe shell of 3.0 ± 0.5 Fe at 3.08 Å ± 0.02 Å (σ = 0.11 Å, Figure 8d). This Fe-Fe distance is consistent with the b dimension calculated from the XRD pattern (b = 9.20 Å) and compares favorably to that obtained for nontronite (3.07 Å). N_{Fe} = 3.0 ± 0.5 is a maximum value as assuming the existence of Si neighbors in the spectral fitting of the hisingerite spectrum would lower the number of nearest Fe atoms. This relatively low number of metal atoms around Fe atoms detected by EXAFS in hisingerite is consistent with the decrease of the signal in both k (EXAFS spectra) and R spaces (RDF) compared to nontronite.

The Fe^{2+}-Me EXAFS contribution of S-2 could also be fitted assuming either one or two metal shells. The former resulted in 6 ± 1Fe at 3.21 ± 0.02 Å (σ = 0.10 Å) and the latter in 6 ± 1Fe at 3.21 ± 0.02 Å (σ = 0.10 Å) + 4 ± 1Si at 3.30 Å ± 0.03 Å (σ = 0.09 Å) (Figures 9a and 9b). In contrast to nontronite, adding a Si shell did not change parameters of the Fe shell. This result is explained by the interference of elementary waves. Figure 9c shows that the wave phase associated with the Si shell is shifted by about $\pi/4$ in the low k range, whereas it superimposes on the Fe shell in the high k range. Thus, adding the Si shell to the theoretical wave causes only a slight shift of its phase, which was readily compensated in the fitting procedure by changing the energy of the threshold origin (ΔE, Teo 1986) by 3 eV. Determining the mineralogical nature of this ferrous-bearing phase is not straightforward and is discussed below.

Si K-EXAFS. Si K-EXAFS spectra and RDF for all samples and nontronite are presented in Figures 6c and 6d and Figures 7c and 7d. Spectra and RDF for S-1 and nontronite have very similar lineshapes, which indicates close similarities of local structures near the

https://doi.org/10.1346/CCMN.1995.0430305 Published online by Cambridge University Press

Si atoms. Fourier filtered Si-(Si, Fe) contributions for S-1 and nontronite are in phase over nearly the entire k span $3.5 \leq k \leq 9$ Å^{-1} (Figure 10a). This indicates that both materials have similar Si-Fe and Si-Si distances. In contrast to Fe K-edge cation contributions to EXAFS (previous section), the presence of two cation shells at distinct distances is now firmly ascertained at the Si K-edge due to the dip in the amplitude at 7 Å^{-1} for nontronite and 8.5 Å^{-1} for S-1. Least-squares fitting resulted in 3.0 ± 0.6Si at 3.03 ± 0.02 Å and 1.5 ± 0.5 Fe at 3.26 ± 0.02 Å (Figure 10b), which is consistent with a phyllosilicate structure (Figure 11).

EXAFS spectra and RDF for S-2 and S-3 are similar, but do not resemble that of nontronite (Figure 6d). Note that Si-rich scales exhibit a single and relatively weak RDF peak attributed to Si-(O, OH) atomic pairs whereas quartz yields two marked peaks (Figure 7d). In quartz, the former at about 1.1 Å (distance not corrected for phase shift) is intense and corresponds to the oxygen coordination about Si atoms. The second peak near 2.2 Å originates from the four Si nearest neighbors across corner-sharing tetrahedra. The intensity reduction of the first RDF peak and the lack of a Si-Si peak in Si-rich scales, relative to quartz, indicate a wider range of interatomic distances and a large spread of interpolyhedra bond angles. In quartz, Si-O-Si bond angles are identical (144°) and the four nearest Si atoms occur at 3.057 Å. But in amorphous silica, Si-O-Si bond angles show variation in angles from 120° to 180°, with a median at 144° (Mozzi and Warre 1969). This variation of angles results in a distribution of Si-Si distances. Electronic waves backscattered by each of Si neighbors are not exactly in phase, and the amplitude of the resulting wave and the corresponding RDF peak are smeared out. The origin of the structural disorder observed in the first coordination shell of Si (Si-O peak) in opal is not clearly understood. Tetrahedra are more rigid than octahedra and many refinements of silicate structures show Si-O distances are within 1.61–1.64 Å (Liebau 1985). Consequently, the observed disorder in A-opal may be related to hydroxyl groups substituted for oxygen in Si tetrahedra. If this substitution exists, Si tetrahedra will be distorted and variations in Si-O bonds would be expected.

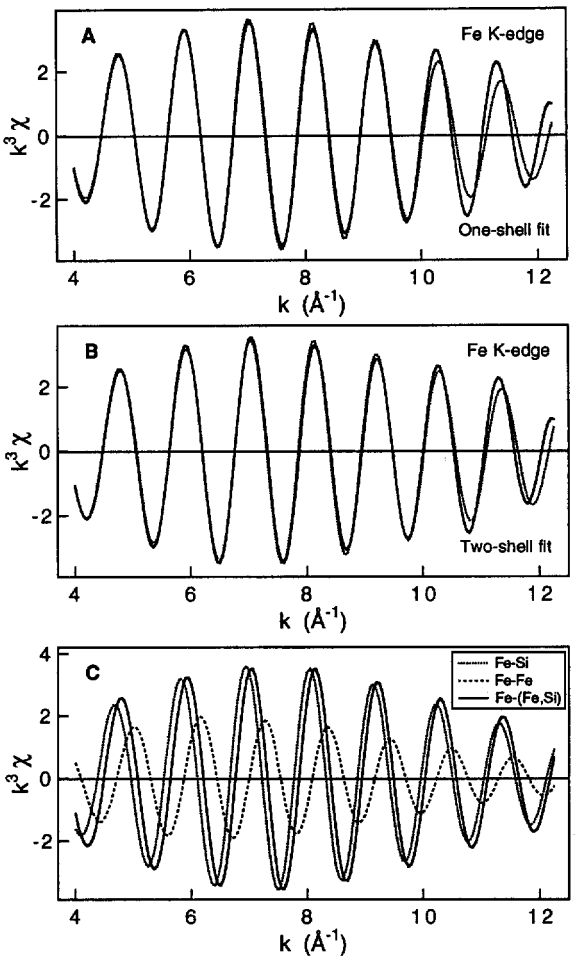

Figure 9. a) and b): Fourier filtered Fe-(Fe, Si) contributions for S-3 (solid line) with simulations (dotted line). c) Comparison of Fe-Fe, Fe-Si and Fe-(Fe, Si) contributions to EXAFS.

DISCUSSION

Structure of hisingerite

The hydrous ferric silicate occurring in high temperature scale deposits at the Salton Sea geothermal field has structural and chemical similarities to hisingerite. Principal structural chemical characteristics of this hydrous silicate are: (1) a Si/Fe ratio close to 1:1, (2) iron presents as Fe^{3+}, (3) a diffraction pattern resembling smectite with turbostratic layer stacking, and (4) an IR spectrum similar to hydrous silicates and providing indirect evidence for Fe-O-Si linkages. Because of its poor crystallinity hisingerite has not been characterized, but suggested structures assignments were proposed previously. Hisingerite was considered an interstratified montmorillonite/chlorite (Lindqvist and Jansson 1962) and a poorly crystallized form of either iron-rich saponite (Whelan and Goldich 1961) or nontronite (Gruner 1935, Sudo and Nakamura 1952, Kohyama and Sudo 1975, McKenzie and Berezowski 1980). Hisingerite is now regarded as a poorly crystalline form of nontronite. This conclusion is supported by the present study. Our study demonstrates that hisingerite and nontronite have the same local organization with the existence of Fe-O-Si linkages as determined by Si K-edge EXAFS.

Hisingerite, however, is not structurally identical to nontronite. For example, its IR spectrum usually does not display the OH bending absorption band at 817 cm^{-1} assigned to Fe^{3+}-OH-Fe^{3+} groups in nontronite.

https://doi.org/10.1346/CCMN.1995.0430305 Published online by Cambridge University Press

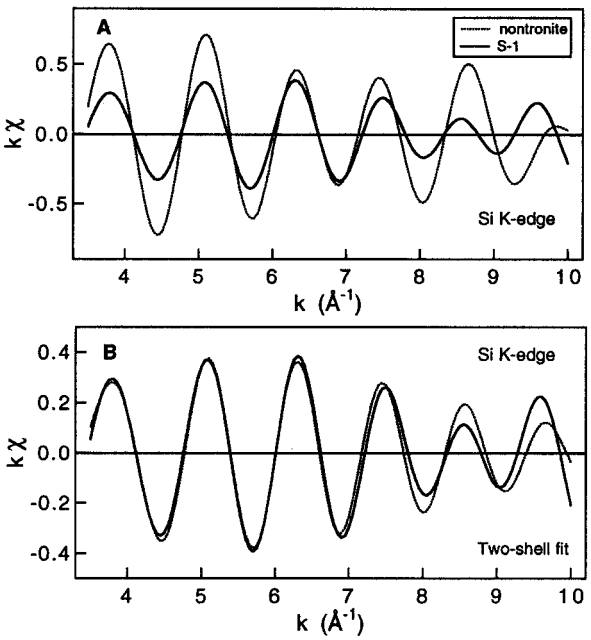

Figure 10. Fourier filtered Si-(Si, Fe) contributions to EXAFS for S-1. (a) Comparison to nontronite; (b) simulation assuming 3.0 ± 0.6Si at 3.03 ± 0.02 Å and 1.5 ± 0.5Fe at 3.26 ± 0.02 Å.

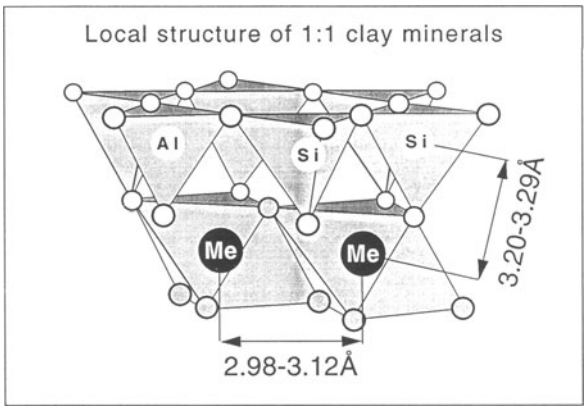

Figure 11. Notion of clay-like local structure. In clays metal atoms are surrounded by 3 (dioctahedral structures) or 6 (trioctahedral structures) nearest cations (Me) at ca. 2.98–3.12 Å and 4 (Si, Al) atoms at ca. 3.20–3.29 Å, the exact distance depending on the chemical composition. A specific feature of this group of minerals is the shortening of the metal-metal distance across edges compared to those in the $Me(OH)_n$, brucite-like, structure. For example, the Mg-Mg distance is equal to 3.06 Å in $Si_4Mg_3O_{10}(OH)_2$ (talc) and 3.12 Å in $Mg(OH)_2$. This shortening results from structural adjustments necessary to adapt the lateral size of octahedral and tetrahedral sheets (Bailey 1984). Correspondingly, two criteria are diagnostic for the existence of a clay-like structure: (i) a Me-Me distance comprised between 2.98–3.12 Å, and (ii) the presence of a (Si, Al) shell near 3.20–3.29 Å. These two criteria are sufficient because they are never simultaneously met in any other silicate structures.

Two explanations are possible. First, this lack of IR absorption feature may be due to the substitution of hydroxyl by fluorine. This is consistent with the high concentration of fluoride in Salton Sea brines (up to 20 mg/kg) even to the point of precipitating fluorite in crystallizer-clarifiers and injection piping below about 130°C (Gallup 1993, Gallup and Featherstone 1994). Second, synthesis experiments have shown that this absorption band is absent from hydrous ferric silicates recently-precipitated or synthesized at low temperature (e.g., 23°C) and progressively appears upon aging or increasing the incubation temperature to ca. 89°C, i.e., upon formation of long-range order (Decarreau *et al* 1987, Farmer *et al* 1991). Structural data obtained for this natural hisingerite are in many respects similar to those reported for synthetic dioctahedral ferric smectites (Decarreau *et al* 1987, Mizutani *et al* 1991, Farmer 1992). For example, the intensity of the second RDF peak for hisingerite is half compared to that of nontronite. The magnitude of this decrease is identical to that found for silico-ferric coprecipitates aged at 150°C for 12 days (Decarreau *et al* 1987). Decarreau *et al* (1987) interpreted this reduced amplitude as related to "border effects," due to the reduced size of the coherent domains compared to well-crystallized nontronite. EXAFS spectroscopy is extremely sensitive to disorder effects, a slight incoherency of atomic distances undergoing a strong reduction of the scattered wave amplitude. This characteristic differs from wide angle X-ray scattering techniques (Eggleton *et al* 1983), which gives a better indication of the distribution of interatomic distances.

In conclusion, laboratory studies show that layer-silicates can nucleate by mixing an iron salt with silicic acid or sodium orthosilicate hydrate at mild temperature. These conditions correspond to those for the deposition of hisingerite at Salton Sea geothermal field.

On the possible confusion between hisingerite and ferrihydrite

Hisingerite and ferrihydrite are distinct minerals, with the former a hydrous silicate and the latter an oxyhydroxide (Chukhrov *et al* 1973). However, both are poorly crystalline with varying amounts of defects. At their most disordered, hisingerite and 2-line ferrihydrite display only two broad XRD bands near 2.6 Å and 1.5 Å (Farmer 1992). The absence of basal reflection in some hisingerites (e.g., McKenzie and Berezowski 1980, Whelan and Goldich 1961) can be related to a lack of stacking periodicity. Recently, Farmer (1992) noted the possible confusion between these "2-line hisingerites" and 2-line ferrihydrite. Farmer questioned the status of "2-line ferrihydrite" by noting the lack of structural evidence proving that this material is a poorly organized form of ferrihydrite, whose mineral nature was accepted in 1975 by the International Mineral-

https://doi.org/10.1346/CCMN.1995.0430305 Published online by Cambridge University Press

ogical Association (Fleischer *et al* 1975). The same criticism was raised by Childs (1992).

Even in their most disordered states, however, XRD traces for pure hisingerite and ferrihydrite are sufficiently distinct to prevent confusion. Figure 12a shows that the XRD pattern for hisingerite contains hk bands which, by definition (Brindley and Brown 1980), are asymmetric towards high angles (see, e.g., the band at 2.6 Å). This asymmetry intrinsically arises from the two-dimensional structure of hisingerite crystallites. In contrast, the asymmetry of the strongest scattering band at 2.5–2.6 Å of 2-line ferrihydrite is reversed from that of hisingerite (Figure 12a). Drits *et al* (1993) showed that this asymmetry is due to hematite impurities in ferrihydrite samples. Patterns of disordered hisingerite also display broad intensity humps near 4.6 Å (corresponding to the 02-11 scattering band of layer silicates) and 3.1 Å not observed in 2-line ferrihydrite. However, the best test for differentiating hisingerite and ferrihydrite is from EXAFS spectroscopy. These materials can be readily differentiated because hisingerite is a layered material and ferrihydrite is a 3D framework structure. Therefore, RDF for hisingerite shows a single metal shell peak from edge-sharing Fe octahedra, whereas the ferrihydrite RDF has two Fe peaks from edge and corner Fe octahedral linkages (Figure 12b, Combes *et al* 1990, Manceau and Drits 1993).

The structural afiliations between 2-line ferrihydrite obtained by hydrolyzing a ferric iron salt solution and ferrihydrite *sensu stricto* was assessed by EXAFS spectroscopy (Manceau and Drits 1993). Both materials possess the same local structure and using the term "2-line ferrihydrite" for designating a poorly crystalline form of ferrihydrite appeared justified. However, we agree with Farmer (1992) that the designation of "amorphous ferric oxide" is preferred for materials whenever structural relationship with true ferrihydrite are not established. We believe, furthermore, that the term "hydrous ferric oxide" is more appropriate because these materials are not truly amorphous, as they

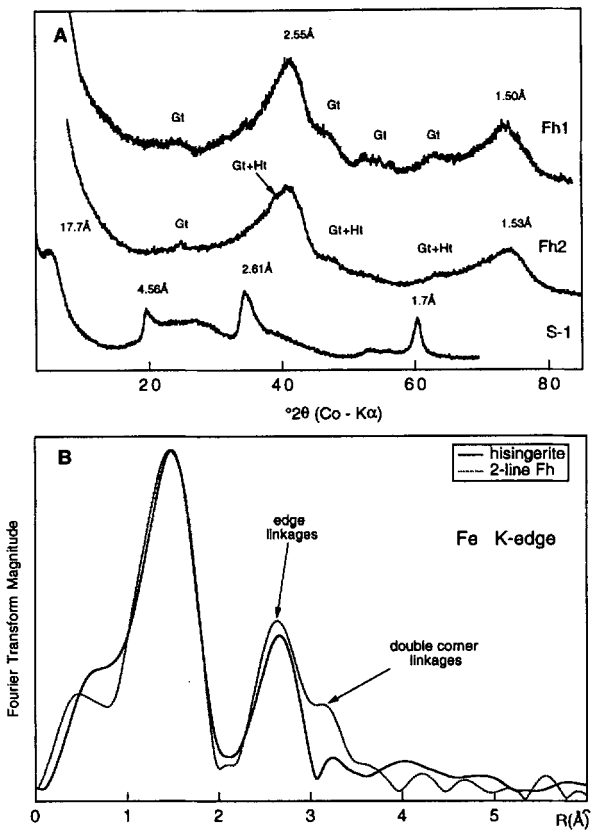

Figure 12. XRD pattern (a) and RDF (b) for hisingerite and 2-line ferrihydrite. The Fh1 sample was obtained by hydrolyzing at pH ≈ 8 a ferric nitrate solution prealably aged during 6 days at pH ≈ 2.5 (OH/Fe = 2.5). Impurities of goethite crystallites are clearly observed and their formation has been favored during the aging at acidic pH (Schwertmann and Murad 1983). The Fh2 sample was synthesized by rapidly hydrolyzing a ferric perchlorate solution. The resulting precipitate was aged 3 weeks at pH 8.2 before drying (Spadini *et al* 1994). The presence of small grains of hematite and goethite is clearly observed, the former impurity being detected by a shoulder at 2.69 Å (arrow). Growth of hematite grains was favored by the aging at neutral pH (Schwertmann and Murad 1983).

Table 3. Structural data for selected iron silicates and ferrobrucite.

	b[1] (Å)	d(Fe-Fe)[2] (Å)	d(Fe-Fe)[3] (Å)	Reference
Nontronite	9.14	3.05	3.08Å	Brindley and Brown (1980) Decarreau *et al* (1987)
S-1	9.20	3.07	3.07Å	This study
Annite	9.33–9.40	3.11–3.13		Donnay *et al* (1964); Hazen and Burnham (1973)
Minnesotaite	9.60	3.20	—	Guggenheim and Eggleton (1986)
Greenalite	9.69	3.23	—	Guggenheim *et al* (1982)
$Fe(OH)_2$	9.78	3.26	—	Coey (1988)
S-3	9.41	3.14	3.21Å	This study

[1] b parameter calculated from d(060).
[2] Calculated from XRD.
[3] Determined by EXAFS.

https://doi.org/10.1346/CCMN.1995.0430305 Published online by Cambridge University Press

Table 4. Mössbauer parameters at room temperature for octahedral Fe^{2+} in various hydrous ferrous silicates and hydroxides.

Sample	δ/Fe	ΔE_Q	W	Intensity %	Reference
Greenalite	1.16	2.75			Coey (1984)
	1.14	2.53	0.42	34	Mizutani *et al* (1991)
	1.06	1.82	0.73	26	
Chlorite	1.12	2.62			Coey (1984)
Minnesotaite	1.15	2.75			Coey (1984)
Talc	1.15	2.63			Noack *et al* (1986)
Brucite	1.15	2.94			Blaauw *et al* (1979)
$Fe(OH)_2$	0.96	2.98			Miyamoto (1976)1

Isomer shift (δ/Fe), Quadrupole splitting (ΔE_Q) and line width (W) given in $mm \cdot s^{-1}$ and relative to iron foil.
1-Original δ value corrected by −0.09 (Blauw *et al* 1979).

have well-ordered structure at the local scale. The name, 2-line ferrihydrite, was used in the literature for designating Si-containing hydrous ferric oxides. This nomenclature is improper since ferrihydrite has no Si atoms, and the presence of tetrahedra in significant number profoundly alters the local structure of 2-line ferrihydrite (Waychunas *et al* 1993), which then loses its structural affinity with ferrihydrite.

Mineralogical nature of the Fe^{2+}-containing phase in Si-rich scales

In contrast to the reasonably well-understood Fe^{3+}-rich scales, the crystal chemical status of iron in sample S-3 is not evident. The XRD trace for S-3 displays a primary maximum at 22–23° 2θ due to opal and two diffuse maxima at 2.6–2.7 Å and 1.57 Å. These latter maxima cannot be attributed to silica since they are not observed in S-2. We believe they result from an ancillary phase and, specifically, to 13-20 and 06-33 bands of a disordered phyllosilicate structure, the 02-11 band being masked by the strong scattering hump of silica. Figure 2 shows that the two *hk* bands are shifted downangle compared to hisingerite. This displacement is attributed to an increase of the *b* unit cell parameters based on Fe^{2+} content (see below).

According to the Mössbauer and EXAFS results, Fe atoms are divalent and coordinated by about 6Fe at 3.21–3.22 Å. Based on topological considerations, these results indicate a layered structure with edge-sharing Fe octahedra. Three mineral structures are possible: ferrobrucite ($Fe(OH)_2$), a 1:1 hydrous iron silicate (greenalite), and a 2:1 hydrous iron silicate such as annite or minnesotaite. Structural data for these minerals are reported in Table 3. Note that the *b* cell parameters increase from Fe^{3+} to Fe^{2+}-containing minerals, but also from 2:1 to 1:1 phyllosilicates and to ferrobrucite. The latter *b* variation is caused by the adjustment of octahedral and tetrahedral sheet dimensions in layer silicates (Brindley and Brown 1980, Bailey 1984). Based on the *b* parameter (≈9.4 Å) and Fe^{2+}-Fe^{2+} distance (≈3.21 Å), the possibility of $Fe(OH)_2$ as the Fe-bearing phase contained in S-3 is rejected. EXAFS results indicate a clay-like structure (Figure 11) and are consistent with either minnesotaite or greenalite. However, their presence cannot be ascertained, and the possibility of an intimate mixture between different phyllosilicates cannot be excluded, as well. This structural interpretation is consistent with the observation of *hk* bands on the XRD trace. The absence of basal reflections, however, probably indicates small crystallite sizes with only a couple of layers. Mössbauer parameters for a selection of minerals are reported in Table 4. Note that the quadrupole splitting for S-3 (Table 2, $\Delta E_Q = 2.59$ $mm \cdot s^{-1}$) is far too small for ferrobrucite ($\Delta E_Q = 2.98$), but agreement is reasonable for the phyllosilicates. In conclusion, Si and Fe atoms partly mix in siliceous scales precipitated at low temperature. This scale deposit is composed of a mixture of opal and micro- and nano-crystallized hydrous ferrous silicate.

Comparison of local order in hydrous ferric and ferrous silicates

The local order about Fe atoms is greater in S-3 than in hisingerite. In S-3, EXAFS detected a coordination of 6 ± 1 around Fe, which indicates that crystallites have a relatively large extension in the *ab* plane. An estimate of the diameter of layers can be calculated (Manceau and Calas 1986) from the average number of nearest metal neighbors since, in trioctahedral structures, internal Fe atoms have 6 nearest cation neighbors, whereas external Fe atoms have only 3 to 4. For an average Fe coordination of 5, a layer size corresponds to ca. 30 Å. Of course, the number of external atoms rapidly decreases as the layer size increases, and sensitivity of the coordination number to the layer size decreases when it exceeds 4 to 5 (Manceau and Calas 1986). Thus, the 30 Å value is only a tentative estimate representing an absolute minimum. In hisingerite, the Fe coordination number is half of nontronite and the layer size evaluated by this method is 10 Å. This difference in crystallinity between ferric and ferrous silicates is noteworthy and can be understood by synthesis experiments. Crystal growth experiments show that reducing environments produce faster growth rates than oxidizing media (Decarreau and Bonnin 1986, 1987, Mizutani *et al* 1991, Farmer *et al* 1994). For example, the time necessary to obtain a ferric smectite

with coherence scattering domains of about 100 Å in size in oxidizing conditions (Fe^{3+} in solution) and at 25°C was estimated at 10 years (Decarreau *et al* 1987). No similar estimation has been reported for ferrous smectite, but data from Decarreau (1987, 1986), Mizutani *et al* (1991), and Farmer *et al* (1994) indicate that this time is much shorter.

Geothermal applications

The present work confirms that different iron-rich siliceous compounds are deposited from Salton Sea brine during fluid manipulation for energy extraction. Variations in structure and chemistry are observed both within and between samples, indicating that fluid composition and temperature varies in both time and space during deposition. The residence time of a fixed volume of brine in higher-temperature process piping is seconds, whereas low-temperature brine residence time in clarifiers is hours. This variation may account for increased crystallinity of hydrous iron silicates.

Deposits formed at high temperature, upstream of scale inhibition processes, consist of hisingerite. Hisingerite formation is slow (typically less than 0.6 cm/year) and generally does not deleteriously affect energy extraction. Scales formed at intermediate temperatures in the brine-handling system are heterogeneous and consist of mixtures of hydrous ferric and ferrous silicates and opal. In the absence of scale control, precipitation from brine occurs at rates exceeding 30 cm/year. When brine is acidified to control scale deposition or reducing agents are added (Gallup 1989), iron precipitation is inhibited whereas silica and an aluminosilicate phase continue to deposit at a rate of less than 1 cm/year. In the crystallizer-reactor clarifier process, brine is reduced in temperature to ~100°C and supersaturated solids are precipitated as sludge. Based on present results, silica and iron that precipitate in the crystallizers and clarifiers at low temperature probably form a ferrous Si-rich clay (i.e., minnesotatite) along with silica precipitates as pure A-opal. Scaling rates observed downstream of the clarifiers in injection piping and injection wells are in the 0.5 cm/year range. This scaling rate may be further reduced by enhancing clay precipitation in the clarifiers with certain reagents or inhibiting opal deposition employing silica scale inhibitors in the injection piping.

CONCLUSION

1. High temperature (250°C) scale precipitated from non-oxidized geothermal brines contain polymerized ferric iron and silica. The mineralogical nature of this precipitate has been identified as hisingerite.

2. Hisingerite is a poorly-crystallized, non-stoichiometric nontronite. As compared to nontronite, hisingerite has no libration OH band detected by IR spectroscopy. This distinctive feature is believed to result from the very small size of crystalline domains.

3. Low temperature (100°C) scale precipitated from non-oxidized geothermal brines consists of a mixture of A-opal and micro- or nano-crystalline hydrous ferrous silicate structurally related to minnesotaite and/or greenalite. These components are difficult to identify by XRD alone.

ACKNOWLEDGMENTS

R. J. Kirkpatrick and B. Montez (University of Illinois, Urbana) are gratefully acknowledged for the NMR spectra. We are indebted to Drs. Bonnin and Morin for acquisition and help in interpretation of Mössbauer spectra. The authors are also grateful to Dr. Stephen Guggenheim and George Kacandes for their valuable review of the manuscript. We thank Unocal Corporation management for permission to publish these results.

REFERENCES

Bailey, S. W. 1984. Crystal chemistry of the true micas. In *Micas.* S. W. Bailey, ed. *Reviews in Mineralogy* **13**: 13–60.

Blaauw, C., G. Stroink, W. Leiper, and M. Zentilli. 1979. Crystal-field properties of Fe in brucite $Mg(OH)_2$. *Phys. Stat. Sol. (b)* **92**: 639–643.

Bonnin, D., G. Calas, H. Suquet, and H. Pezerat. 1985. Sites occupancy of Fe3+ in Garfield nontronite. *Phys. Chem. Miner.* **12**: 55–64.

Brigatti, M. F. 1982. Hisingerite: A review of its crystal chemistry. In *Development in Sedimentology,* 35. H. Van Olphen and F. Veniale, eds. Int. Clay Conf. Bologna and Pavia 1981. Amsterdam: Elsevier, 97–110.

Brindley, G. W., and G. Brown. 1980. Crystal structures of clay minerals and their X-ray identification. London: Mineralogical Society, 495 pp.

Cardile, C. M., and J. H. Johnson. 1985. Structural studies of nontronites with different iron contents by ^{57}Fe Mössbauer spectroscopy. *Clays & Clay Miner.* **33**: 295–300.

Carlson, L., and U. Schwertmann. 1981. Natural ferrihydrites in surface deposits from Finland and their association with silica. *Geochim. Cosmochim. Acta* **45**: 421–429.

Childs, C. W. 1992. Ferrihydrite: A review of structure, properties and occurrence in relation to soils. *Z. Pflanzenernärh. Bodenk.* **155**: 441–448.

Childs, C. W., N. Matsue, and N. Yoshinaga. 1990. Ferrihydrite deposits in Paddy Races, Aso-Dani. *Clay Sci.* **8**: 9–15.

Chukhrov, F. V., B. B. Zvyagin, A. I. Gorshkov, L. Ermilova, and V. V. Balashova. 1973. Ferrihydrite. *Izvest. Akad. Nauk. SSSR (Ser. Geol.)* **4**: 23–33 (Russian). Trans. in *Int. Geol. Rev.* **16**: 1131–1143.

Coey, J. M. D. 1984. Mössbauer spectroscopy of silicate minerals. In *Mössbauer Spectroscopy Applied to Inorganic Chemistry.* S. Long, ed. Plenum Press, 443–509.

Coey, J. M. D. 1988. Magnetic properties of iron in soil iron oxides and clay minerals. In *Iron in Soils and Clay Minerals.* J. W. Stucki, B. A. Goodman, and U. Schwertmann, eds. NATO ASI series **217**: 397–466.

Combes, J. M., A. Manceau, and G. Calas. 1990. Formation of ferric oxides from aqueous solutions: a polyhedral approach by X-ray absorption spectroscopy. II. Hematite formation from ferric gels. *Geochim. Cosmochim. Acta* **54**: 1083–1091.

Decarreau, A., and D. Bonnin. 1986. Synthesis and crystallogenesis at low temperature of Fe(III)-smectites by evo-

lution of coprecipitated gels: Experiments in partially reducing conditions. *Clay Miner.* **21**: 861–877.

Decarreau, A., D. Bonnin, D. Badaut-Trauth, R. Couty, and P. Kaiser. 1987. Synthesis and crystallogenesis of ferric smectite by evolution of Si-Fe coprecipitates in oxidizing conditions. *Clay Miner.* **22**: 207–223.

De Jong, B. H. W. S., J. Van Hoek, W. S. Veeman, and D. V. Mason. 1987. X-ray diffraction and ^{29}Si magic angle-spinning NMR of opals: Incoherent long- and short-range order in opal-CT. *Amer. Mineral.* **72**: 1195–1203.

Donnay, G., N. Morimoto, H. Takeda, and J. D. H. Donnay. 1964. Trioctahedral one-layer micas. I. Crystal structure of a synthetic iron mica. *Acta Cryst.* **17**: 1369–1373.

Drits, V. A., B. A. Sakharov, A. L. Salyn, and A. Manceau. 1993. Structural model for ferrihydrite. *Clay Miner.* **28**: 185–208.

Eggleton, R. A. 1977. Nontronite: Chemistry and X-ray diffraction. *Clay Miner.* **12**: 181–194.

Eggleton, R. A. 1988. The application of micro-beam methods to iron minerals in soils. In *Iron in Soils and Clay Minerals.* J. W. Stucki, B. A. Goodman, and U. Schwertmann, eds. NATO ASI series **217**: 165–201.

Eggleton, R. A., J. H. Pennington, R. S. Freeman, and I. M. Threadgold. 1983. Structural aspects of hisingerite-neotecite series. *Clay Miner.* **18**: 21–31.

Farmer, V. C. 1991. Possible confusion between so-called ferrihydrites and hisingerites. *Clay Miner.* **27**: 373–378.

Farmer, V. C., G. S. R. Krishnamurti, and P. M. Huang. 1991. Synthetic allophane and layer-silicate formation in SiO_2-Al_2O_3-FeO-Fe_2O_3-MgO-H_2O systems at 23°C and 89°C in a calcareous environment. *Clays & Clay Miner.* 39: 561–571.

Farmer, V. C., W. J. McHardy, F. Elsass, and M. Robert. 1994. *hk*-ordering in aluminous nontronite and saponite synthesized near 90°C: Effects of synthesis conditions on nontronite composition and ordering. *Clays & Clay Miner.* **42**: 180–186.

Fleischer, M., G. Y. Chao, and A. Kato. 1975. New mineral names: Ferrihydrite (M.F.). *Amer. Mineral.* **60**: 485–486.

Gallup, D. L. 1989. Iron silicate scale formation and inhibition at the Salton Sea geothermal field. *Geothermics* **18**: 97–103.

Gallup, D. L. 1993. The use of reducing agents for control of ferric silicate scale deposition. *Geothermics* **22**: 39–48.

Gallup, D. L., and J. L. Featherstone. 1994. Control of NORM deposition from Salton Sea geothermal brines. *Geotherm. Sci. & Tech.* **8**: 1–12.

Gallup, D. L., and W. M. Reiff. 1991. Characterization of geothermal scale deposits by Fe-57 Mössbauer spectroscopy and complementary X-ray diffraction and infra-red studies. *Geothermics* **20**: 207–224.

Goodman, B. A., J. D. Russell, A. R. Fraser, and F. W. D. Woodhams. 1976. A Mössbauer and IR spectroscopic study of the structure of nontronite. *Clays & Clay Miner.* **24**: 53–59.

Gruner, J. W. 1935. The structural relationship of nontronite and montmorillonite. *Amer. Mineral.* **20**: 475–483.

Guggenheim, S., S. W. Bailey, R. A. Eggleton, and P. Wilkes. 1982. Structural aspects of greenalite and related minerals. *Can. Min.* **20**: 1–18.

Guggenheim, S., and R. A. Eggleton. 1986. Structural modulations in iron rich and magnesium rich minerals. *Can. Miner.* **24**: 477–497.

Hazen, R. M., and C. W. Burnham. 1973. The crystal structures of one-layer phlogopite and annite. *Amer. Mineral.* **58**: 889–900.

Hoyer, D., K. Kitz, and D. Gallup. 1991. Salton Sea Unit 2. Innovations and successes. *Geo. Res. Council Trans.* **15**: 355–361.

Kohyama, N., and T. Sudo. 1975. Hisingerite occurring as a weathering product of iron-rich saponite. *Clays & Clay Miner.* **23**: 215–218.

Liebau, F. 1985. *Structural Chemistry of Silicates. Structure, Bonding, and Classification.* Berlin, Springer-Verlag.

Lindqvist, B., and S. Jansson. 1962. On the crystal chemistry of hisingerite. *Amer. Mineral.* **47**: 1356–1362.

Lippmaa, E., M. Magi, A. Samoson, G. Engelhardt, and A. R. Grimmer. 1980. Structural studies of silicates by solid-state high resolution ^{29}Si NMR. *J. Amer. Chem. Soc.* **102**: 7606–7607.

Manceau, A. 1990. Distribution of cations among the octahedra of phyllosilicates: Insight from EXAFS. *Can. Miner.* **28**: 321–328.

Manceau, A., D. Bonnin, P. Kaiser, and C. Frétigny. 1988. Polarized EXAFS of biotite and chlorite. *Phys. Chem. Miner.* **16**: 180–185.

Manceau, A., D. Bonnin, W. E. E. Stone, and J. Sanz. 1990. Distribution of Fe in the octahedral sheet of trioctahedral micas by polarized EXAFS. Comparison with NMR results. *Phys. Chem. Miner.* **17**: 363–370.

Manceau, A., and G. Calas. 1986. Ni-bearing clay minerals. 2. X-ray absorption study of Ni-Mg distribution. *Clay Miner.* **21**: 341–360.

Manceau, A., and V. A. Drits. 1993. Local structure of ferrihydrite and feroxyhite by EXAFS spectroscopy. *Clay Miner.* **28**: 165–184.

McKale, A. G., B. W. Veal, A. P. Paulikas, S. K. Chan, and G. S. Knapp. 1988. Improved ab initio calculations for extended absorption fine structure spectroscopy. *J. Amer. Chem. Soc.* **110**: 3763–3768.

McKenzie, K. J. D., and R. M. Berezowski. 1980. Thermal and Mössbauer studies of iron-containing hydrous silicates. II. Hisingerite. *Thermochim. Acta* **41**: 335–355.

Milkey, R. G. 1960. Infrared spectra of some tectosilicates. *Amer. Mineral.* **45**: 990–1007.

Miyamoto, H. 1976. The magnetic properties of $Fe(OH)_2$. *Mat. Res. Bull.* **11**: 329–336.

Mizutani, T., Y. Fukushima, A. Okada, O. Kamigaito, and T. Kobayashi. 1991. Synthesis of 1:1 and 2:1 iron phyllosilicates and characterization of their iron state by Mössbauer spectroscopy. *Clay & Clay Miner.* 39: 381–386.

Moenke, H. H. W. 1974. Silica, the three-dimensional silicates, borosilicates, and beryllium silicates. In *The Infrared Spectra of Minerals.* V. C. Farmer, ed. *Mineralogical Society Monograph* **4**: 365–382.

Mozzi, R. L., and B. E. Warre. 1969. The structure of Vitreous Silica. *J. Appl. Cryst.* **2**: 164–172.

Müller, D., W. Gessner, H. J. Behrens, and G. Scheler. 1981. Determination of the aluminium coordination in aluminium-oxygen compounds by solid-state high resolution ^{27}Al NMR. *Chem. Phys. Letters* **79**: 59–62.

Noack, Y., A. Decarreau, and A. Manceau. 1986. Spectroscopic and isotopic evidence for low and high temperature origin of talc. *Bull. Miner.* **109**: 253–263.

Oles, A., A. Szytula, and A. Wanic. 1970. Neutron diffraction study of γFeOOH. *Phys. Status Solidi* **41**: 173–177.

Rozenson, I., and L. Heller-Kallai. 1977. Mössbauer spectra of dioctahedral smectites. *Clays & Clay Miner.* **25**: 94–101.

Schwertmann, U., and E. Murad. 1983. The effect of pH on the formation of goethite and hematite from ferrihydrite. *Clay & Clay Miner.* **31**: 277–284.

Schwertmann, U., and H. Thalmann. 1976. The influence of [Fe(II)], [Si], and pH on the formation of lepidocrocite and ferrihydrite during oxidation of aqueous $FeCl_2$ solutions. *Clay Miner.* **11**: 189–199.

Shayan, A. 1984. Hisingerite material from a basalt quarry near Geelong, Victoria, Australia. *Clay & Clay Miner.* **32**: 272–278.

Spadini, L., A. Manceau, P. W. Schindler, and L. Charlet. 1994. Structure and stability of Cd^{2+} surface complexes on ferric oxides. *J. Coll. Interf. Sci.* (in press).

Sudo, T., and T. Nakamura. 1952. Hisingerite from Jaan. *Amer. Mineral.* **37**: 618–621.

Teo, B. K. 1986. *EXAFS: Basic Principles and Data Analysis. Inorganic Chemistry Concepts 9.* Berlin, Springer-Verlag, 369 pp.

Vempati, R. K., and R. H. Loepert. 1985. Structure and transformation of siliceous ferrihydrites. American Society of Agronomy Annual Meeting. *Agron. Abstracts,* 152.

Vempati, R. K., and R. H. Loepert. 1989. Influence of structural and adsorbed Si on the transformation of synthetic ferrihydrite. *Clay & Clay Miner.* **37**: 273–279.

Waychunas, G. A., B. A. Rea, C. C. Fuller, and J. A. Davis. 1993. Surface chemistry of ferrihydrite: Part 1. EXAFS studies of the geometry of coprecipitated and adsorbed arsenate. *Geochim. Cosmochim. Acta* **57**: 2251–2269.

Webb, J. A., and B. L. Finlayson. 1987. Incorporation of Al, Mg, and water in opal-A: Evidence from speleothems. *Amer, Mineral.* **72**: 1204–1210.

Whelan, J. A., and S. S. Goldich. 1961. New data for hisingerite and neotocite. *Amer. Mineral.* **46**: 1412–1423.

(Received 8 July 1994; accepted 21 October 1994; MS 2536)